Zhuang *et al. Biochar* (2024) 6:11
https://doi.org/10.1007/s42773-024-00302-9

Biochar

ORIGINAL RESEARCH Open Access

Preparation of biochar adsorption material from walnut shell by supercritical CO_2 pretreatment

Zitong Zhuang[1], Yanbing Liu[1], Wenwen Wei[1], Jinwen Shi[1] and Hui Jin[1*]

Abstract

In order to treat dyes in the wastewater of the printing industry and to reutilize walnut shell (WS) waste generate economic benefits, supercritical carbon dioxide (SC-CO_2) pretreatment technology was developed to prepare porous biochar as a precursor for adsorption material. Orthogonal experiments were conducted at the temperatures of 200, 300, and 400 ℃ with durations of 20, 40, and 60 min, and a control group was set up using N_2 pretreatment. Then, KOH activation was employed to prepare biochar adsorption material. The biochars were analyzed and characterized using TGA, BET, SEM, FT-IR, and XRD, and the liquid and gas phase products of the pretreatment process were analyzed semi-quantitatively and quantitatively using GC–MS and gas chromatography. Methylene blue (MB) dye was selected as an indicator to measure the adsorption capacity of biochar, and adsorption kinetics were analyzed based on the data. The results indicate that pretreatment with SC-CO_2 effectively enhanced the performance and yield of the activated carbon. The highest specific surface area increased by 18%, and the maximum adsorption of MB increased by 23% compared to the N_2 control group. The yield increased by 8–262% and the specific surface area increased by 50–192% compared to the direct activation of walnut shell (WS). During the pretreatment processes for the preparation of biochar adsorption material with the best specific surface area, phenol-enriched bio-oil was produced as a by-product which has economic value.

Highlights

1) The poly-generation of biochar precursor and bio-oil could be realized by supercritical CO_2.
2) Prepared activated carbon had great physical performance and excellent dye adsorption capacity.
3) The pretreatment process produced high-value organic liquid by-products.
4) Mild pretreatment conditions were more advantageous.

Keywords Supercritical carbon dioxide, Walnut shell, Biochar, Methylene blue adsorption

Handling editor: Xing Yang.

*Correspondence:
Hui Jin
jinhui@mail.xjtu.edu.cn
Full list of author information is available at the end of the article

Graphical Abstract

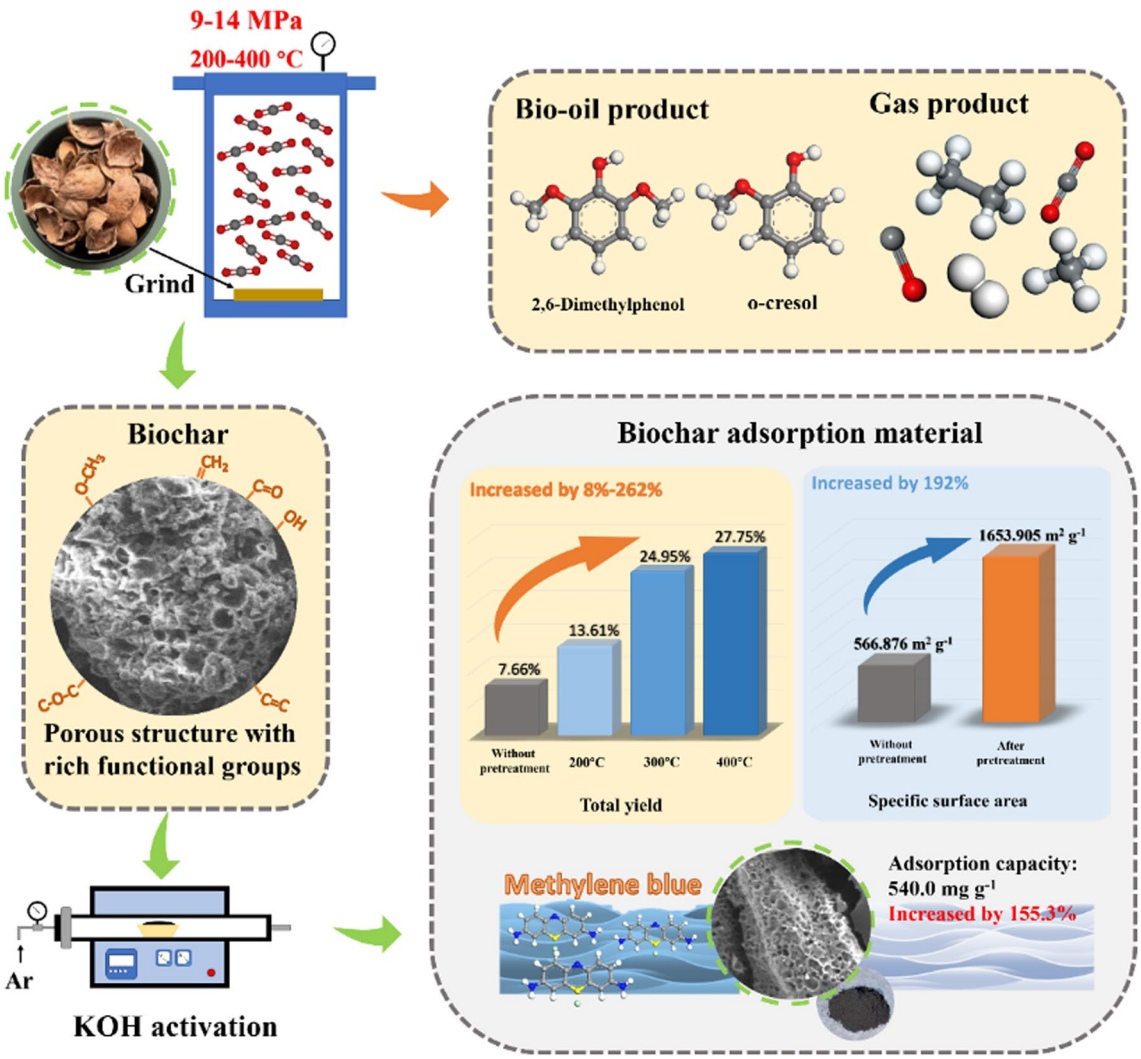

1 Introduction

In recent years, several industries have been discharging incompletely treated industrial wastewater directly into the ecosystem, causing serious environmental problems (Mashkoor and Nasar 2020). Methylene blue (MB) is widely used in dyestuffs, chemical indicators, and biopharmaceuticals. It is commonly found in industrial wastewater and can be used as a representative organic pollutant in wastewater (Santoso et al. 2020). Activated carbon (AC) has become a popular choice as an adsorbent for MB removal from wastewater (Rafatullah et al. 2010). Commercial AC mainly uses precursors such as petroleum residues, coal, peat, and lignite, which are expensive and non-renewable feedstocks (Yahya et al. 2015). Therefore, in addition to substituting petroleum-derived products, a number of ways of converting and utilizing agricultural waste are being explored to achieve environmental protection and economic benefits (González-García 2018). Biomass feedstocks are diverse and renewable, and plant biomass is one of the world's most abundant and underutilized biological resources (Naik et al. 2010). In recent decades, scientists around the world have been researching and developing various biomasses for the preparation of ACs and testing their MB adsorption capacities. El-Bery et al. (2022) activated lignin waste to prepare AC with a specific surface area of 1771 $m^2\ g^{-1}$ and measured its capacity to absorb MB as 148.8 mg g^{-1}. Egbosiuba et al. (2020) prepared AC with

a specific surface area of up to 2114 $m^2\ g^{-1}$ using ultrasound-assisted activation of fruit wastes, and its MB adsorption capacity was measured to be 196 mg g^{-1}. It was reported that mixing fox nutshell with $ZnCl_2$ prepared AC with an astonishing specific surface area of 2869 $m^2\ g^{-1}$ and an adsorption capacity of 249.88 mg g^{-1} for MB (Kumar and Jena 2016).

China's walnut industry has experienced rapid development. As of the end of 2020, China's walnut production reached 1.1 million tons, accounting for 33.1% of the world's total walnut production (Yan et al. 2022), and substantial production of walnuts has led to a significant abundance of WSs as a by-product. However, the current utilization of walnut shells remains relatively low, resulting in significant resource wastage. WSs are characterized by their high lignin content, hard and porous texture, large surface area, and low cost. Utilizing WSs as biomass feedstock for carbon production not only enables the resource utilization of waste WSs but also reduces the cost of preparing AC. As a result, the application prospects for using WSs as a carbonaceous biomass material are very promising. Liu and Zhang (2023) used WS to prepare polyaminated walnut shells using $K_2S_2O_8$/$NaHSO_3$ as an inducer and ring-opening treatment. Shi et al. (2023) prepared AC with a specific surface area of 1713.87 $m^2\ g^{-1}$ using one-step activation of walnut shells and illustrated its strong adsorption capacity for tetracycline. Yang et al. (2022) prepared AC by activating WSs modified with $ZnCl_2$ aided by light waves and microwaves and tested the adsorption properties with acidic magenta.

Supercritical carbon dioxide (SC-CO_2) is an easily accessible, non-toxic, non-flammable, and cost-effective solvent that does not contaminate the products. CO_2 has a relatively low critical temperature (31.1℃) and pressure (73.8 bar). Therefore, compared to other solvents, the energy requirement for achieving supercritical fluid conditions with CO_2 is relatively low (Wang et al. 2024). Under SC-CO_2 pressure, the small pores in biomass expand due to the increased diffusion characteristics, enabling effective mass transfer, making it an excellent reaction medium for the preparation of porous biochar (Badgujar et al. 2021). Because of these excellent properties of SC-CO_2, there have been numerous reports on the treatment of biomass under SC-CO_2 atmosphere nowadays. For example, Albarelli et al. (2011) used SC-CO_2 treatment on banana peel waste to produce biochar. They found that the biochar exhibited a rich microporous structure and studied its performance through Cu ion adsorption experiments. Jiang et al. (2022a) utilized a high-pressure CO_2-hydrothermal method to extract water charcoal as a precursor for AC from banana pseudostems. Gao et al. (2010) utilized SC-CO_2 pretreatment to enhance the conversion of rice straw biomass. Zhang and Wu (2014) conducted a study where they used subcritical CO_2 to treat sugarcane bagasse. The research findings revealed that the use of subcritical CO_2 effectively removed hemicellulose from the raw material, leading to improved digestibility of the sugarcane bagasse. Zhou et al. (2023) conducted a comparative study on the gasification yield of rice husk by SC-CO_2, the gas yield and carbon gasification rate of rice husk gasification were found to be higher compared to an Ar atmosphere. While these studies all utilized only a single property of SC-CO_2, such as using it for the extraction of organics, and employing SC-CO_2 as a solvent or a reactant, without considering the combined effect of these two properties. In this paper, the multiple properties of SC-CO_2 were used to treat biomass waste to achieve poly-generation, i.e., the production of porous char precursors for AC while simultaneously producing high-value organic by-products.

Although there have been many reports on the preparation of biomass-based AC as well as SC-CO_2 treatment of biomass, there is a lack of poly-generation technology that can utilize CO_2 and biomass energy more rationally and efficiently. In this study, we utilized SC-CO_2 pretreatment of WSs as the core strategy for converting biomass into biochar precursors, which can be further processed into high-performance AC. Additionally, this method simultaneously produced a valuable phenol-rich bio-oil by-product. In order to judge the feasibility of this preparation route for large-scale application, the pretreatment yield and AC yield were calculated and the solid products were characterized using TGA, BET, SEM, XRD, FT-IR, and elemental analyses, as well as the types and contents of the products in the gas and liquid phases. Finally, the adsorption capacity of the prepared AC was also determined using MB dye, which is commonly found in the effluents of printing and dyeing industries. The findings of this study provide a promising and sustainable strategy for the large-scale reutilization of CO_2 and WSs waste and for the treatment of dyeing industrial wastewater.

2 Feedstock and methods

2.1 Feedstock

Walnut shells, purchased from Henan Province, were ground using a grinder after being dried for 48 h. They were then filtered through a 150-mesh sieve and dried in an oven at 105 ℃ until the quality no longer changed. The elemental analysis of the feedstock was carried out with the Vari Macro elemental analyzer manufactured by Elementar Corporation, and the proximate analysis of the sample was analyzed by SDTGA5000 produced by Sande Corporation. The results are shown in Table 1.

Table 1 Elemental and proximate analysis of walnut shell

Sample	Elemental analysis (wt%)					Proximate analysis (wt%)			
	C	H	N	S	O[a]	M_{ad}	A_{ad}	V_{ad}	FC_{ad}
WS	50.130	6.613	1.240	0.509	41.508	0.92	0.74	79.96	18.38

ad air drying base

[a] By difference

2.2 Preparation of biomass char

All experiments were carried out in a batch reactor made of iron-nickel alloy, which was in the shape of tube closed at one end, and had a size of 1cm i.d.×15 cm length. The pressure and temperature that the reactor can withstand are 30 MPa and 750 ℃, respectively. In each experiment, the heating furnace was heated to the predetermined temperature in advance, and then the reactor was put into the heating furnace to reach the predetermined temperature before timing. For each reaction, 2 g of dried WSs powder was introduced. Before the reaction, the reactor was purged with CO_2 to remove the air and placed in a thermostatic water tank. The initial reaction temperature and pressure were set at 60 ℃ and 7.8 MPa, respectively, to maintain the reactants within a SC-CO_2 environment throughout the process. The temperature rise rate of the reactor was 10 ℃ min^{-1} and the final pressures were 9–14 MPa. A control group was established with reactions conducted under an N_2 atmosphere. Research has indicated that reaction pressure significantly influences the outcomes of biomass pyrolysis, while the quantity of gases does not impact the results (Hanaoka et al. 2012; Morais et al. 2015), so the control group was maintained at the same pressure as the experimental group when reaching the reaction temperature. Following an orthogonal experimental design, experiments were conducted at the reaction temperatures of 200 ℃, 300 ℃, and 400 ℃, coupled with reaction times of 20 min, 40 min, and 60 min.

Once the reaction reached the designated time, the reactor was taken out from the heating furnace quickly and cooled in a water pail. After the reactor had cooled to the initial temperature, the gas was collected with air air bags. Then, the liquid product was collected after each reaction and was extracted into 40 mL of dichloromethane in order to determine the liquid phase products by GC–MS. At the same time, the solid product could be obtained after liquid phase filtration. The solid product was dried in an oven at 105 ℃ for 48 h to obtain char. The samples were named according to the reaction conditions as C(N)x/y, where C indicates reactions conducted within a SC-CO_2 atmosphere, and N signifies N_2 atmosphere. The variables x and y represent the reaction temperature and reaction time, respectively. For example, C200/20 is the sample which was reacted at 200 ℃ for 20 min in the SC-CO_2 atmosphere.

The yield of char is as follows:

$$Y_{char} = \frac{m_{solid}}{m_{WS}} \times 100\%, \tag{1}$$

where m_{solid} is the mass of the solid product, g, and m_{WS} is the mass of WS powder fed into the reactor, g.

2.3 Preparation of activated carbon

0.8 g of char and 2.4 g of KOH were added to 20 mL of ultrapure water, stirred with a magnetic stirrer at 500 r min^{-1} for 2 h, so that the char and KOH were fully mixed, and placed in a vacuum oven at 105 ℃ for drying for 24 h, obtaining char-KOH mixed powder. The mixed powder was placed in a tube furnace and passed through Ar as a protective gas at 100 mL min^{-1} and heated up to 700 ℃ at a heating rate of 10 ℃ min^{-1} and maintained for 60 min. After cooling to room temperature, it was washed with 0.1 mol L^{-1} hydrochloric acid to remove KOH, and centrifuged at 4000 r min^{-1}. The supernatant was extracted and the ultrapure water was added for another round of centrifugation. The process was repeated until the solution achieved a neutral PH. The solid obtained from filtration was dried in an oven at 105 ℃ for 24 h. This activated carbon was labeled as C(N)x/y-AC, for instance, C200/20-AC, where AC indicates activated carbon. Specifically, the AC produced by activating WS feedstocks without the pretreatment by SC-CO_2 was designated as WS-AC. This sample was as the control group for comparison.

The yield of the activation process and the total yield of the treatment are calculated as follows:

$$Y_{AC} = \frac{m_{AC}}{m_{char}} \times 100\%, \tag{2}$$

$$Y_{total} = Y_{char} \times Y_{AC}, \tag{3}$$

where m_{AC} is the mass of the AC after drying, g, and m_{char} is the mass of the char before activation, g, and Y_{total} represents the total yield of AC produced from treated WSs, %.

2.4 Methods of analysis

The gasification characteristics of samples in N_2 atmosphere at 50 mL min^{-1} were observed by STA449F3 thermogravimetric analyzer manufactured by NETZSCH company. In the process of thermogravimetric analysis (TGA), 11 mg of sample was used for each test, and the temperature rose from 50 ℃ to 800 ℃ at the rate of 10 ℃ min^{-1}. The study was conducted using a sample-free crucible as a blank group to prevent the effects of buoyancy and crucible differences in the experiment. Calibrated thermogravimetric curves were calculated by subtracting the curves from the blank experiment from the curves obtained when the samples were tested. The liquid products were analyzed using Agilent's 7890GC-MS instrument. Before testing, the dichloromethane extract of the liquid products was diluted fivefold with dichloromethane. Then, 1 mL of the diluted solution was filtered through a 0.45 μm filter nozzle and added to a specialized vial for the instrument. The vial was placed in the instrument for extraction and analysis. Compound analysis was performed using the NIST17 mass spectral library retrieval. Qualitative analysis of the liquid products in each test was conducted by comparing the peak area ratios of individual components.

Gas composition in the gas products was analyzed using the Agilent 7890 gas chromatograph, manufactured by Agilent Technologies. Furthermore, the volumes of various gas components in the gas products were quantitatively calculated by comparing them to the composition ratios of standard mixed gases.

The surface morphology of the solid product was observed and analyzed by Superscan SSX-550 SEM–EDX manufactured by Shimadzu Corporation.

The surface area and pore structure of the samples were analyzed using the ASAP2460 fully automated surface area and pore size analyzer, manufactured by Micromeritics. The measurements were conducted at a temperature of 77 K using N_2 adsorption–desorption data. Subsequently, the specific surface area was calculated using the BET theory based on the adsorption isotherms of the samples. Before gas adsorption measurements, the samples were subjected to a 12-h degassing process at 150 °C under vacuum using the VacPrep instrument.

The crystal structure of the solid sample was measured using an X'pert Pro X-ray diffractometer (XRD) from Panacor, The Netherlands. XRD is an analytical instrument that uses the X-ray principle to study the internal structure of a substance. The target of the XRD used was CuKα, and the operating voltage and current were 40 kV and 40 mA, respectively. The scanning rate was 8.85° min^{-1}, and the scanning range was 5–80°. In order to further analyze the XRD results, the lamellar diameters (L_a) and stacking heights (L_c) of the aromatic lamellae as well as the layer spacing (d_{002}) were then calculated according to the Scherrer and Braggs formula (Eqs. 4–6):

$$L_a = \frac{1.84\times\lambda}{\beta_{100}\times\cos\theta_{100}}, \tag{4}$$

$$L_c = \frac{0.89\times\lambda}{\beta_{002}\times\cos\theta_{002}}, \tag{5}$$

$$d_{002} = \frac{\lambda}{2\times \sin\theta_{002}}, \tag{6}$$

where λ is the wavelength of the X-ray, nm, β is the FWHM width of the diffraction peak, and θ is the diffraction angle, °.

The functional groups in the solid products were analyzed using a Fourier-transform infrared spectrometer (FT-IR) from Bruker, model Vertex70. The spectral analysis was conducted in the range of 400–4000 cm^{-1}, with a resolution of 4 cm^{-1}. Background scans were performed 32 times, and the sample scans were conducted 128 times.

The UV–visible spectrophotometer model DR6000 from HACH was utilized. At the wavelength (665 nm) corresponding to the maximum absorbance value of the MB solution, the absorbance value was measured. This measurement was used to calculate the solution's concentration and the adsorption capacity of the feedstocks for MB.

The results of the three-phase product were quantified to obtain the distribution of carbon elements in the three-phase product. The results of the elemental analysis were multiplied by the mass of the char to obtain the carbon content in the solids:

$$CC_s = \frac{m_{char}\times\omega_{char}}{M_C}, \tag{7}$$

where CC_s is the carbon content in the solid product, mol , m_{char} is the mass of the prepared char, g , ω_{char} is the carbon content in the char determined by an elemental analyzer, % and M_c is the relative atomic mass of the element carbon, g mol^{-1}.

The carbon content of the gas was determined by first measuring the gas components using gas chromatograph, quantitatively calculating the carbon content of the gas-phase product based on the calibration mixture gas, and subtracting the carbon content of the initial CO_2 admittance.

$$CC_g = \sum n_i \times \omega_i - CC_{in}, \tag{8}$$

where CC_g is the carbon content in the gas product, mol, n_i is the molar mass of a gas, mol, ω_i is the elemental carbon content in the corresponding gas, %, and CC_{in} is the carbon content in the initially passed CO_2, mol.

The carbon content in the liquid phase was calculated based on the conservation of the element carbon, using the carbon content of the feedstocks minus the carbon content of the solid and gas phase.

$$CC_l = \frac{m_{WS} \times \omega_{WS}}{M_C} - CC_s - CC_g, \tag{9}$$

where CC_l is the carbon content in the liquid product, mol, m_{WS} is the mass of input WS, g, ω_{WS} is the carbon content of WS measured by the elemental analyzer, %, and M_c is the relative atomic mass of the element carbon, g mol^{-1}.

2.5 Methylene blue adsorption experiment

A series of MB solutions were prepared with concentrations of 0.1, 0.5, 1, 2.5, 3, and 5 mg L^{-1}. The absorbance values at a wavelength of 665 nm were measured using a UV–visible spectrophotometer and used to plot a concentration standard curve:

$$C = 4.8193x - 0.1928, \tag{10}$$

where C is the concentration of MB, mg L^{-1}, x is the absorbance value at 665 nm.

50 mg of AC was put into 300 mL of MB solution with a concentration of 100 mg L^{-1} and stirred using a magnetic stirrer at 1000 r min^{-1}. The solution was withdrawn at the 1st, 2nd, 3rd, 5th, 10th, 15th, 30th, 80th, 120th, 240th, and 1440th minutes and filtered through a 0.45 μm filter nozzle, and the resultant solution was measured by the UV spectrophotometer at 665 nm.

The adsorption capacity of MB per unit mass of AC at time t, mg g^{-1}:

$$q_t = \frac{(C_0 - C_t) \times V}{m_{AC}}, \tag{11}$$

where $C_0$is the initial concentration of MB, mg L^{-1} , C_t is the concentration at time t, mg L^{-1} , V represents the volume of the solution, L , and m_{AC} stands for the mass of introduced AC, g.

Perform first-order and second-order adsorption kinetics analysis based on the adsorption capacity of AC for MB. The pseudo-first-order equation (Eq. 12) and the pseudo-second-order equation (Eq. 13) are as follows:

$$\lg(q_e - q_t) = \lg q_e - \left(\frac{k_1}{2.303}\right) \times t, \tag{12}$$

where q_e represents the equilibrium adsorption capacity of AC for MB, mg g^{-1}, q_t is the adsorption capacity of MB at time t, mg g^{-1}, and k_1 is the rate constant for pseudo-first-order adsorption, min^{-1}.

$$\frac{t}{q_t} = \frac{1}{k_2 \times q_e^2} + \frac{t}{q_e}, \tag{13}$$

where q_e is the equilibrium adsorption capacity of AC for MB, mg g^{-1}, q_t is the adsorption capacity of MB at time t, mg g^{-1}, and k_2 is the rate constant for pseudo-first-order adsorption, g mg^{-1} min^{-1}.

In order to study the mechanism of adsorption of MB by AC and to understand the type of adsorption steps controlling the adsorption, intraparticle diffusion (Eq. 14) was equally used for the study.

$$q_t = K_p \times t^{0.5} + C, \tag{14}$$

where q_t is the amount adsorbed at time t, mg g^{-1} , K_p is the rate constant for intra-particle diffusion, mg $min^{0.5}$ g^{-1} , and C represents the adsorption capacity, mg g^{-1}, which is related to the thickness of the boundary layer.

3 Results and discussion

3.1 Thermogravimetric analysis (TGA)

Thermogravimetric analysis (Fig. 1) was carried out on the experimental and control char samples obtained after the pretreatment to investigate the composition of the char. Each sample showed a small weight loss peak at around 70 ℃, which was a drying peak due to water loss. Hemicellulose is thermally unstable and starts to decompose at 250–330 ℃, cellulose decomposes in a narrow temperature range of 300–400 ℃. Lignin decomposes over a wide temperature range of 250–550 ℃ (Wang et al. 2020). It can be seen that the weight loss peak of hemicellulose was not present in any of the conditions, suggesting that the hemicellulose was completely decomposed after the pretreatment. At a pretreatment temperature of 200 ℃, the weight loss peak of cellulose was present in all of the N_2 atmosphere controls, however, in the SC-CO_2 atmosphere only the sample with the shortest pretreatment time still had a weight loss peak of cellulose, which indicated that cellulose was no longer present within the C200/40 and C200/60, proving that the SC-CO_2 condition promoted cellulose decomposition. Except for the 200/20 condition, the lignin peaks in the char produced under the SC-CO_2 condition were significantly higher than those in the control group treated under the N_2 condition. This suggested a higher lignin content in char by SC-CO_2 pretreatment. At the same pretreatment time, the weight loss peaks for lignin at 300 ℃ were all higher than those at 200 ℃, also indicating the increase in the relative content of lignin in the char samples at this time, this was due to the decomposition of cellulose. The weight loss peaks were all very weak under the pretreatment condition of 400 ℃, indicating that most of the original hemicellulose, cellulose, and lignin of the biomass had already been carbonized at this time, and that only a small amount of lignin was left. From the TG curves, the

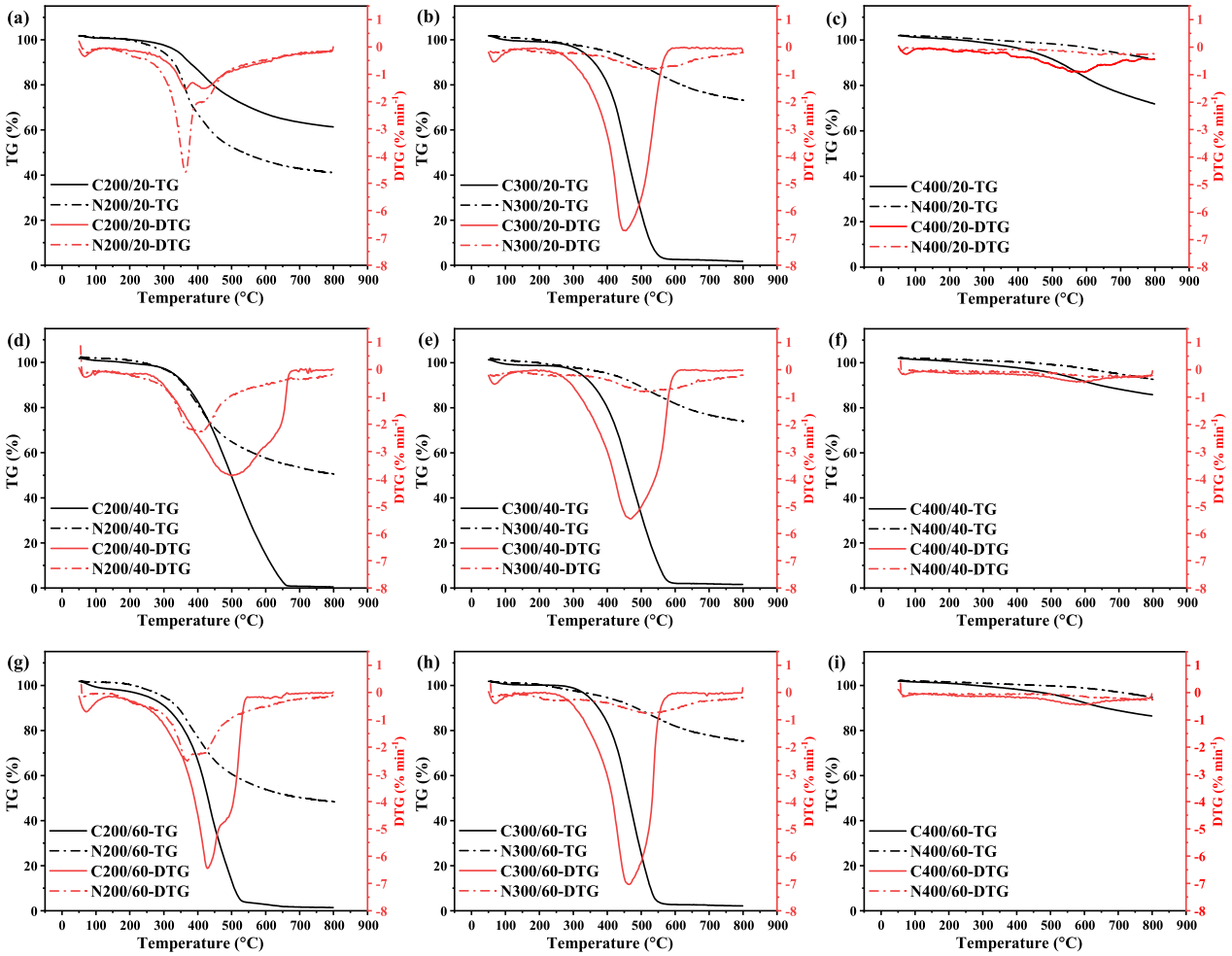

Fig. 1 TG and DTG curves of chars under SC-CO_2 and N_2 pretreatment. **a** Pretreatment at 200 ℃ for 20 min **b** Pretreatment at 300 ℃ for 20 min **c** Pretreatment at 400 ℃ for 20 min **d** Pretreatment at 200 ℃ for 40 min **e** Pretreatment at 300 ℃ for 40 min **f** Pretreatment at 400 ℃ for 40 min **g** Pretreatment at 200 ℃ for 60 min **h** Pretreatment at 300 ℃ for 60 min **i** Pretreatment at 400 ℃ for 60 min

chars pretreated with SC-CO_2 lost more mass than N_2 under all conditions except 200 ℃ for 20 min. This made the SC-CO_2 pretreated chars more reactive than the N_2 pretreated ones in the subsequent KOH activation. From the figures, it was observed that char of 400 °C had lost less mass than at 200 and 300 °C, because of the presence of ordered carbon structures (Om Prakash et al. 2020).

3.2 Biochar yields

The calculated char yields, activation yields, and total yields are given in Fig. 2. The total yields of AC prepared by the pretreatment step followed by activation were all higher than the yields of WS-AC (7.67%) which was activated directly with WS. As the pretreatment temperature increased, the yields of char showed a decreasing trend, which was consistent with the conclusion obtained from thermogravimetric analysis that the decomposition of hemicellulose, cellulose, and lignin was more adequate as the temperature increased. The yields of the activation increased as the pretreatment temperature increased. In particular, the activation yields of samples with a pretreatment temperature of 300 ℃ increased dramatically compared to 200 ℃, whereas the activation yields of samples pretreated at 400 ℃ showed a reduced increase compared to 300 ℃. There are two possible reasons for this difference in growth rate. Firstly, the decomposition of cellulose lignin in biomass is not yet sufficient at the lower pretreatment temperatures (Zhao et al. 2017), and they continue to pyrolyze during activation causing rapid mass loss. Secondly, the increase of temperature in the pretreatment process can effectively improve the thermal stability of char (Yi et al. 2022), resulting in a higher yield in the high temperature activation process. The total yield also increased with the rise in pretreatment temperature because of the increase in the yield of the activation step. At the same pretreatment temperature, with increasing

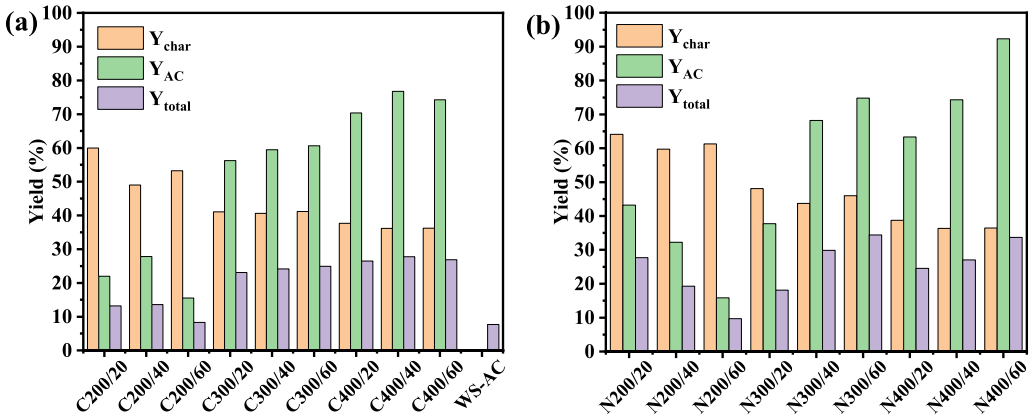

Fig. 2 Char yield, activation yield, and total yield at each pretreatment condition. **a** SC-CO_2 atmosphere **b** N_2 atmosphere

reaction time, there was an initial decrease followed by an increase in char production. This phenomenon can be attributed to the fact that during the pyrolysis process, the extended reaction time at high-pressure conditions enhanced the reaction rate, promoting the cracking of tar into char and gases (Hanaoka et al. 2012).

The results showed that the yields of char during pretreatment in the SC-CO_2 atmosphere were lower than that of the control group. Zhu et al. (2017) attributed this to two reasons: CO_2 reacted with tar, thus inhibiting secondary char formation, and CO_2 might also react directly with char. Farrow et al. (2015) who studied the effect of CO_2 on biomass pyrolysis using a drop tube furnace also demonstrated that CO_2 promoted the gasification of biomass more than N_2, which led to a decrease in char production.

3.3 Elemental analysis

Elemental analysis of the produced char precursors as well as AC was determined (Table 2) and the corresponding O/C and H/C values were calculated. The carbon content in the char samples increased with increasing

Table 2 Elemental analysis of char under SC-CO_2 and N_2 atmosphere

Sample	Elemental analysis (wt%)					O/C	H/C
	C	H	O[a]	N	S		
C200/20	63.080	4.559	29.461	1.010	1.890	0.467	0.072
C200/40	66.380	4.468	27.068	1.000	1.084	0.408	0.067
C200/60	65.510	4.443	28.531	1.010	0.506	0.436	0.068
C300/20	77.550	3.641	17.394	1.060	0.355	0.224	0.047
C300/40	78.700	3.889	15.734	1.370	0.307	0.200	0.049
C300/60	79.200	3.696	15.420	1.390	0.294	0.195	0.047
C400/20	85.050	3.228	9.880	1.380	0.462	0.116	0.038
C400/40	86.720	3.467	7.654	1.830	0.329	0.088	0.040
C400/60	86.930	3.243	7.778	1.690	0.359	0.089	0.037
N200/20	63.820	4.347	30.335	1.280	0.218	0.475	0.068
N200/40	67.560	4.613	26.202	1.410	0.215	0.388	0.068
N200/60	65.630	4.726	27.964	1.500	0.180	0.426	0.072
N300/20	76.590	3.920	17.783	1.510	0.197	0.232	0.051
N300/40	77.200	3.891	17.205	1.520	0.184	0.223	0.050
N300/60	76.370	3.895	18.123	1.420	0.192	0.237	0.051
N400/20	89.190	3.208	5.539	1.720	0.343	0.062	0.036
N400/40	87.500	2.839	7.542	1.830	0.289	0.086	0.032
N400/60	90.120	3.077	4.613	1.880	0.310	0.051	0.034

[a] By difference

pretreatment temperature and treatment time, indicating that increasing temperature promotes the carbonization reaction. H and O content decreased with the increase of temperature and treatment time . This was due to the biomass pyrolysis process. Moreore and more liquid phase organic compounds and H, O-containing gases were produced, and took away the H, O elements in the solid. As the treatment temperature rose, the O-containing functional groups on the solid surface were also destroyed. For example, the carbon content of C400/60 increased by 79.8% relative to the WS feedstock, while the O and H content decreased by 88.9% and 53.5%, respectively. The measured C content of the pretreated char in the SC-CO_2 atmosphere was lower than that of the N_2 control at 200 and 400 ℃ for all reaction times, while the oxygen content (except for 20 min at 200 ℃) was higher than that of the N_2 control. However, the results were reversed at a pretreatment temperature of 300 ℃, with the experimental group having a higher C content than the control group and a lower O content. This suggested that SC-CO_2 as a reaction atmosphere at 300 ℃ produced a more carbon-rich char by promoting deoxygenation and dehydrogenation reactions (Yi et al. 2022). The ratios of O/C and H/C were also calculated, and the ratio of O/C in the SC-CO_2 treated samples was higher than that of the control at 200 ℃ and 400 ℃, and lower at 300 ℃, with a similar pattern for the H/C values. This indicated that the char was more aromatic at 300 ℃, and the stability of char was higher under this condition, which can explain the analysis of thermal stability of samples in thermogravimetric analysis to some extent. Balahmar and Mokaya (2019) suggested that the pores produced in AC and the ease of activation were correlated with the O/C ratio in the char, with char precursors with a low O/C being more difficult to activate by KOH, a trend that is demonstrated in subsequent BET analyses. It can also be argued that char with a higher oxygen content indicated that it had more O-containing functional groups. These complex char compositions served as carriers for KOH activation, facilitating the generation of more complex pore structures and thus increasing the specific surface area. In addition to this, the more oxygenated char was consumed more due to the reaction of KOH with the reactive oxygenated substances in the biomass, and the effect of KOH was significantly enhanced at high temperatures, a finding that was verified in the yield of the activation process. The values of O/C in the C200 samples decreased and then increased with the increase in pretreatment time, while the values of O/C in the C300 samples decreased consistently. Similarly, the values of O/C in the C400 samples also decreased and then increased. Correspondingly, the yields of the activation process for C200-AC increased and then decreased. The activation yields for C300-AC increased with the increasing pretreatment time of the samples, and the activation yields for C400-AC initially increased and then decreased. Elemental analysis of the AC (shown in Additional file 1: Table S1) prepared after activation was also conducted, and the results indicated that the carbon content of the AC increased further. This increase can be attributed to two factors: further carbonization of the sample following the high-temperature activation treatment and the removal of some ash through the washing process used to eliminate KOH after activation. Additionally, the oxygen content of the activated samples decreased, indicating the reaction with KOH.

3.4 Three-phase products

The gas-phase products and liquid-phase products of the experimental group (SC-CO_2 atmosphere) were analyzed specifically and quantitatively, and the carbon content of the three-phase products was calculated. Figure 3 plots the types and yields of gas products under each pretreatment condition. During the pretreatment process, in general, the total amount of gas-phase products showed an upward trend with the increase of pretreatment temperature (Butterman and Castaldi 2010) and it increased from 1.324 mol kg^{-1} at C200/20 to 10.450 mol kg^{-1} at C400/60. As the temperature increased, the variety of gas products began to expand, with H_2, CO, CO_2, CH_4, and C_2H_6 appearing at higher temperatures (300 and 400 ℃). The amount of H_2, as well as low-molecular-weight hydrocarbons (CH_4 and C_2H_6), increased with temperature. Pyrolysis of cellulose at low temperatures (below 300 ℃) involved a reduction in molecular weight and the release of CO and CO_2. At higher temperatures, the molecules rapidly depolymerized, and the disproportionation and decarboxylation of the dehydrated sugar compound

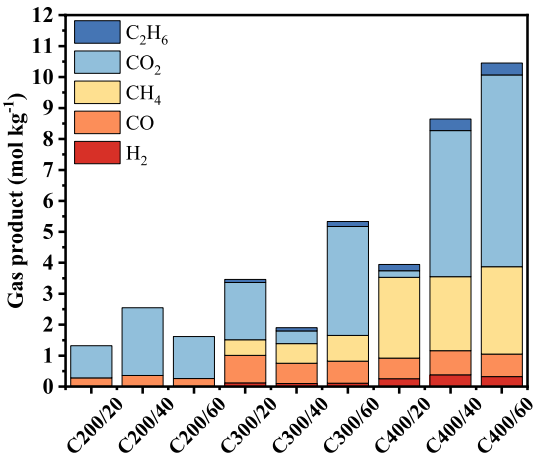

Fig. 3 Types and contents of gases produced by pretreatment

units resulted in a mixture of low-molecular-weight gases and volatile products (Shafizadeh 1982). Meanwhile, secondary reactions of the tar at high temperatures also cracked low molecular weight gases and carbon-containing gas compounds.

The liquid phase products were analyzed using gas chromatography-mass spectrometry (GC–MS) and the compounds corresponding to each peak were retrieved from the database, the spectral lines are shown in Fig. 4, and the relative contents corresponding to some of the compounds were calculated. It can be observed that the liquid products mainly consist of small-molecule compounds, such as 3-methyl-phenol; 2-methoxy-phenol; 2, 6-dimethoxy-phenol; 3, 4-dimethyl-phenol. And monomeric compounds formed during the decomposition of lignin, such as syringylacetone ($C_{11}H_{14}O_4$). The relative percentage content of each compound in the liquid phase product can be obtained by smoothing the spectrum given by GC–MS, and then integrating and normalizing the area of each peak. The detailed peak time of some substances, the corresponding formulas, and the relative contents in the liquid phase products are listed in Table 3.

From the results, as the pretreatment temperature increased from 200 ℃ to 400 ℃, the peak value of the substance in the liquid product gradually decreased, and combined with the trend of the amount of gas and solid products with the pretreatment temperature, it can be concluded that the increase in temperature is more favorable to the gasification of biomass. And as the pretreatment temperature increased, the variety of liquid-phase products began to increase and convert from molecules with high carbon content to small-molecule aromatic compounds with low carbon content. In particular, it should be noted that at the lower treatment temperature of 200 ℃, the type and content of the liquid substances changed regularly with the treatment time, and it was possible to discern from this the evolutionary pattern of the partial decomposition of lignin. Aromatic methoxylation of lignin was stable at low-temperature pyrolysis, with fewer types of pyrolysis products, and lignin first depolymerized into the intermediate (Tan et al. 2022), primary pyrolysis then produced small-molecule aromatic compounds, mainly 2-methoxyphenol (NO. 3 in Table 3) from the fractured lignin guaiacyl and 2,6-dimethoxy-phenol (NO. 8) from the syringy (Liu et al. 2008). The levels of both increased from 13.47% and 19.83% at 20 min to 24.15% and 40.13% at 60 min, respectively. The content of phenol (NO. 1) and 1-(4-hydroxy-3-methoxyphenyl)-2-Propanone (NO. 9) and 1,2-dimethyl-Naphtho[2,1-b] furan (NO. 11)

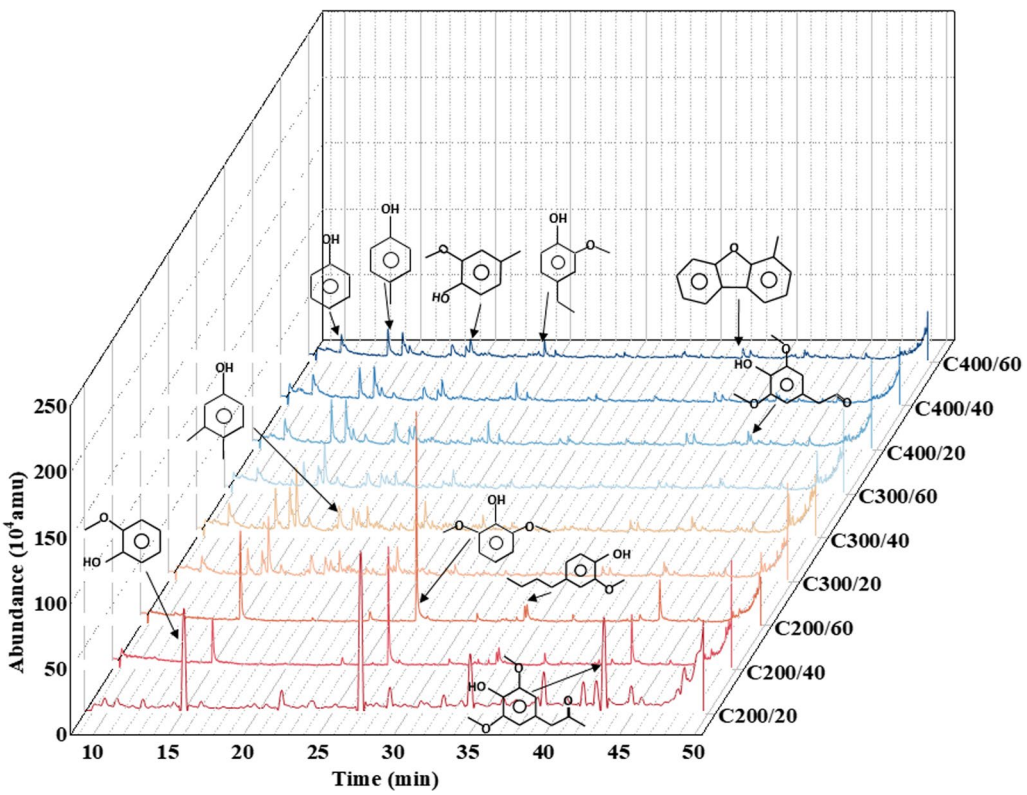

Fig. 4 GC–MS results of liquid products of SC-CO_2 pretreatment under different conditions

Table 3 Appearance time and percentage content of liquid products

No.	Compound	Content (%)								
		C200/20	C200/40	C200/60	C300/20	C300/40	C300/60	C400/20	C400/40	C400/60
1	Phenol	1.09	0.89	0.23	2.04	5.62	2.76	3.96	13.33	5.25
2	2-methyl-phenol	0.21	–	0.20	4.94	4.90	5.09	8.37	9.01	9.45
3	2-methoxy-phenol	13.47	16.82	24.15	12.11	8.70	9.12	3.44	1.88	1.93
4	2,5-dimethyl-phenol	–	–	–	7.40	5.67	5.98	5.49	4.43	7.16
5	3,4-dimethyl-phenol	0.11	–	–	4.77	4.27	2.67	3.31	2.59	3.73
6	Creosol	–	0.19	–	3.39	3.01	2.48	3.74	6.38	7.55
7	4-ethyl-2-methoxy-phenol	0.58	8.23	2.70	4.52	4.75	2.60	2.06	0.69	4.12
8	2,6-dimethoxy-phenol	19.83	30.81	40.13	0.97	0.68	0.61	–	0.19	0.27
9	1-(4-hydroxy-3-methoxyphenyl)-2-propanone	6.26	4.24	2.90	0.74	0.38	0.55	0.52	0.52	0.60
10	6H-Dibenzo[b,d]-pyran	–	3.19	1.41	1.91	1.23	1.46	1.87	2.34	3.15
11	1,2-dimethyl-Naphtho[2,1-b]furan	2.84	2.06	1.37	1.70	1.48	1.27	1.56	1.70	1.51
12	Syringyacetone	11.10	13.29	10.25	0.21	–	0.22	0.86	0.69	0.75
13	Dibutyl phthalate	2.32	1.74	1.18	–	0.30	0.24	–	0.30	0.21
	Phenol content	35.29	56.75	67.41	36.75	34.59	28.83	26.63	32.12	31.91

–: not detected

decreased with pretreatment time. At higher temperatures (400 ℃), a secondary pyrolysis reaction occurred, leading to the cleavage of -O-CH_3 on the aromatic ring, resulting in the formation of phenol and methylphenols (Kawamoto 2017). Thus, it was possible to observe an increase in the content of the corresponding compounds at 400 ℃ (NO.1, NO.2, NO.6 in the Table 3). It was encouraging to note that phenol-enriched by-product with high percentage content up to 67.41% at 200 ℃ appeared, which has some economic value. Particularly, there was 2,6-dimethoxy-phenol with a percentage content of 40.13% at 60 min, which has certain applications in organic synthesis and pharmaceutical research and can be used as a flavor.

Figure 5 shows the calculated distribution of carbon in the three-phase products. An increase in the carbon content of the gas with increasing pretreatment time can be seen at the temperature of 200 ℃, because the pyrolysis of the biomass produced char, tars, and gases, and the cracking reaction of the tars also produced gases (Liu et al. 2018) . Both reactions produced CO and CO_2 at the beginning and grew with reaction time. Interestingly, at pretreatment temperatures of 300 and 400 ℃, the carbon content in the solid-phase product remained essentially constant, while the carbon in the gas and liquid products was constantly changing, suggesting that at this point the reaction of carbon consumption by biomass pyrolysis was in equilibrium with that of the production of secondary coke from tar. The conversion of carbon-containing compounds in the gas and liquid phases was mainly involved during this period.

3.5 Functional groups of char

To further investigate the effect of different pretreatment conditions on the chemical composition of the char, the functional groups of the char were demonstrated using

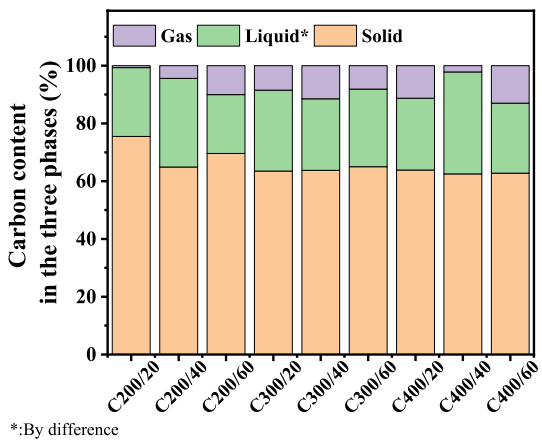

Fig. 5 Content of elemental carbon in three-phase products

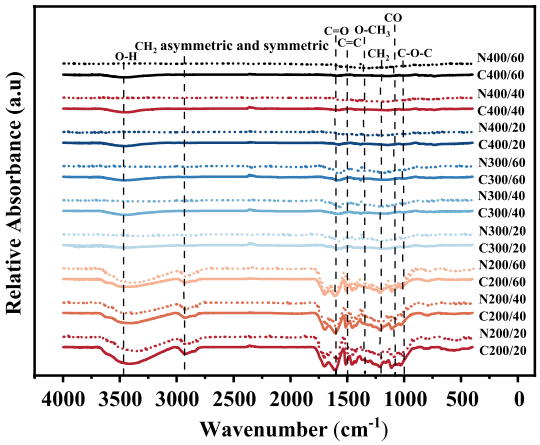

Fig. 6 FT-IR spectra of char in SC-CO_2 and N_2 atmosphere

Fourier transform infrared spectroscopy (FT-IR). The measurements are shown in Fig. 6, and Additional file 1: Table S2 lists the typical functional groups and the corresponding compounds and sources (Zhao et al. 2017; Wang et al. 2021; Yi et al. 2022). The structure of the functional groups was richest at 200 ℃ pretreatment temperature and remained essentially unchanged as the pretreatment time increased. They included C–O–C stretching vibrational peaks (1095 cm^{-1}, 1031 cm^{-1}) present in glycosidic, phenols, ethers, and esters groups, C–O–C asymmetric stretching peak (1153 cm^{-1}) from pyranose ring, C-O stretching peak (1210 cm^{-1}) from Phenol and C=C stretching peak (1600 cm^{-1}) from Aromatic skeletal present in lignin. C=O stretching peak (1695 cm^{-1}) from aldehydes, and CH_2 asymmetric and symmetric stretching peaks (2970–2840 cm^{-1}) from alkyl, aliphatic, and aromatic. The absorption peaks appearing at the 3600–3000 cm^{-1} spectral band were caused by O–H stretching vibrations. Peaks associated with cellulose, such as the –CH_2 wagging peak (1320 cm^{-1}), C–O–C asymmetric stretching peak in pyranose ring (1153 cm^{-1}), and C–O–C stretching peak (1031 cm^{-1}), disappeared after pretreatment at 300 and 400 ℃, indicating complete decomposition, which is consistent with the result obtained from thermogravimetric analysis. The C=C vibrational peaks at 1600 and 1510 cm^{-1} originating from lignin and extractives decreased or even disappeared as the pretreatment temperature increased, representing that the decomposition of lignin tended to be complete with increasing temperature. The O–H vibration peak was also noteworthy, as it was observed in all samples treated under SC-CO_2 atmospheres but was only present in the 200 ℃ samples under the N_2 atmosphere. This indicated that the presence of SC-CO_2 protected the hydroxyl group from

degradation. Chars obtained at low temperature and in the SC-CO_2 atmosphere were richer in oxygen-containing functional groups, which provided more chemically active sites for char precursors (Xiao et al. 2018), and it provided a platform for attaching KOH for activation and could improve the effectiveness of the activation step.

3.6 Characterization of carbon stack structures

The XRD spectra of the char (Fig. 7a) showed that the chars all had graphitic features, and the spectral lines had two distinct peaks as peak 002 (2θ = 22–25°) and peak 100 (2θ = 42–45°). The peak 002 represented the parallelism and stacking height of the aromatic lamellae, and the appearance of peak 002 was mainly attributed to the parallel stacking of the aromatic lamellae. Peak 100 represented the lateral size of aromatic layers, which was the diameter of the layers. The appearance of peak 100 was mainly attributed to the ordered arrangement of carbon atoms in the graphite-like phase within a single plane. Two distinct reflections were also observed in the samples of WS and C200/20: 101 and 040. These were attributable to the the exhibited cellulose structure, indicating partial pyrolysis of cellulose under these conditions, which was consistent with the results of thermogravimetric analysis. At the pretreatment temperature of 200 ℃, with the increasing pre-treatment time, these peaks gradually decreased in intensity and broadened. At this point, aromatic layers coexisted with the cellulose crystal structure, char became a 'continuum' of carbonaceous molecules, involving crystalline and amorphous phases (Pusceddu et al. 2017). At temperatures exceeding 300 ℃, these peaks disappeared entirely, indicating the complete loss of the cellulose crystal structure. Correspondingly, the intensities of the peak 002 and peak 100 increased. These small graphene structures were referred to as disordered microcrystals and continued to develop as the degree of carbonization deepened (Keiluweit et al. 2010). In Origin 2021 software, Gaussian fitting was applied to the 002 and 100 peaks. For the peak 002, a fit with two Gaussian functions was employed, while the peak 100 was fitted with a single Gaussian function. As shown in Additional file 1: Fig. S1, the fitting results were demonstrated using the C400/60 sample as an example. Within the peak 002, there was an additional γ peak (~ 20°), which contributed to the asymmetry of the 002 peak. The appearance of the γ peak was attributed to the presence of alkyl side chains and other structures connected to the edges of the aromatic rings, causing asymmetry in the 002 peak (Jiang et al. 2019).

Additional file 1: Table S3 shows the calculated geometry of the aromatic layers. L_a and L_c can reflect microcrystal sizes. From the results, the calculated lamellar diameters L_a of char did not exhibit any consistent patterns related to pretreatment temperature and time but fluctuated between 1.638 nm and 3.002 nm. The stacking heights of the layers L_c, showed an overall decreasing trend as the pretreatment temperature increased. It decreased from 2.821 nm in C200/20 to 1.399 nm in C400/60. This indicated that the aromatic structures underwent significant lateral aggregation and transformation into polycyclic aromatic hydrocarbons. The d_{002} spacing decreased from the range of 1.556–1.597 nm at 200 ℃ to 1.413–1.458 nm, indicating a reduction in the char's aromatic layer spacing at temperatures exceeding 200 ℃. This suggested that the aromatic layers within the char continued to condense, and at this point, the microcrystalline structure was increasingly tending towards graphitization (Jiang et al. 2019). X-ray diffraction (XRD) spectra of AC were also measured to determine its structure (Fig. 7b). The XRD spectra of AC exhibited 002 and

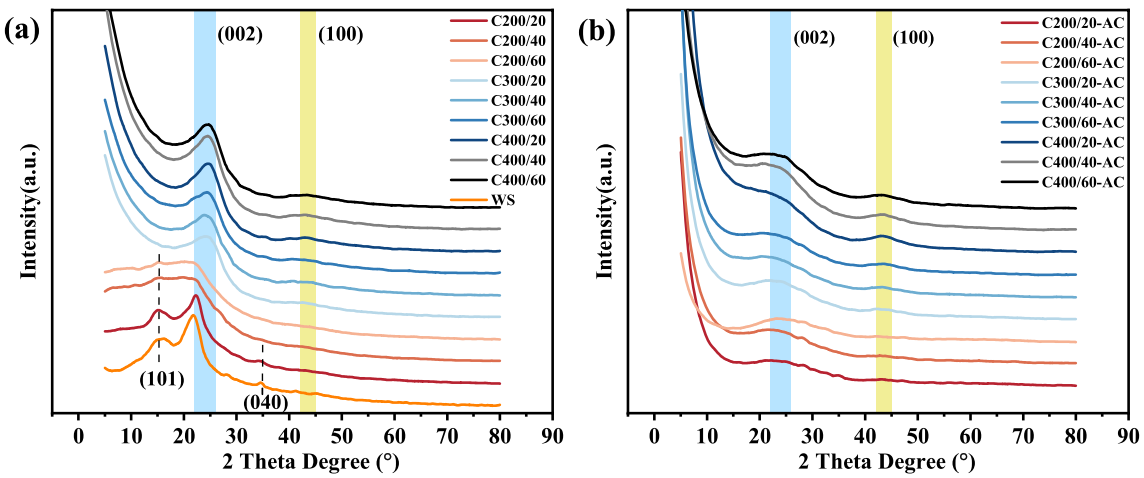

Fig. 7 XRD curves of samples. **a** Char and WS feedstock **b** Activated carbon

100 peaks at 2θ = 22–25° and 2θ = 42–45°, respectively, corresponding to the stacking structure of graphene. However, compared to the 002 and 100 peaks of char, the peaks of AC were weaker and broader. This suggested that the graphene structure of AC had been disrupted, consistent with the destructive property of the activation process. These broad peaks indicated the amorphous nature of the carbon structure, characteristic of typical KOH-AC.

3.7 Porosity analysis

From the electron microscope scanning results (Fig. 8), the external structural morphologies of the biomass after the pretreatment and activation steps were dramatically changed. The structure of the WS feedstock showed irregular lumpy particles with a relatively flat surface and no visible pore structure. After SC-CO_2 pretreatment, the surface of the char material became uneven and rough, revealing abundant honeycomb-like pore structures. This transformation was attributed to the pyrolysis of hemicellulose, cellulose, lignin, and the subsequent release of gases. After the activation step, the AC also exhibited plentiful pores, but the number and shape of the pores differed somewhat from those of the pretreated char. The number of surface pores on the AC increased notably, forming a more compact honeycomb-like pore structure with significantly smaller pore diameters. These microporous structures were removed during the KOH activation carbon gasification process.

To further investigate the pore structure of char and AC, the prepared samples were characterized using N_2 as an adsorbent and a fully automated specific surface area and porosity analyzer. The data obtained are shown in Additional file 1: Table S4. It was evident that the specific surface areas of the pretreated char were relatively low. Under pretreatment temperatures of 200 ℃ and 300 ℃ for a short duration, there was a slight increase in specific surface area compared to the WS feedstocks. However, at 300 ℃ for an extended duration and at 400 ℃, the specific surface areas of the char were even lower than that of the WS. There could be two reasons for this. Firstly, at high temperatures, the tar generated may clog the pore structures. Secondly, after prolonged exposure to high temperatures, the micro-pore structure formed by the char expanded and collapsed, resulting in the narrowing and closure of pore entrances.

In contrast, the specific surface areas of the AC significantly increased. Among the char precursors subjected to SC-CO_2 pretreatment, the highest specific surface area after activation was achieved at 200 ℃ for 20 min, reaching 1653.905 $m^2\ g^{-1}$. During this condition, the pretreatment was the mildest, making it safer and more energy-efficient. The lowest specific surface area was observed at 400 ℃ for 40 min, reaching 848.954 $m^2\ g^{-1}$. With the increase of pretreatment temperature, the specific surface area showed a decreasing trend, which was consistent with the results predicted by FTIR spectral analysis. And with the increase of temperature, the oxygen-containing functional groups of char were continuously destroyed, resulting in the decrease of its chemical active sites, which was not favorable for the attachment of KOH. In comparison, the specific surface area of the AC obtained after the N_2 control treatment had the highest of 1403.690 $m^2\ g^{-1}$, while the lowest was only 0.923 $m^2\ g^{-1}$, which was much lower than that of the AC obtained after the SC-CO_2 treatment. It is noteworthy that the specific surface area of the AC prepared from WS feedstocks without the pretreatment process was only 566.876 $m^2\ g^{-1}$, which was lower than that of all ACs prepared after SC-CO_2 pretreatment. Therefore, although the pretreatment with SC-CO_2 could not increase the specific surface area of the char significantly, and in some cases, it even had a negative impact on the pore structure of the char, the pretreatment provided chemically active sites and made the surface of the char rougher, which allowed more KOH to be attached to the carbon surface and improved the effect of activation.

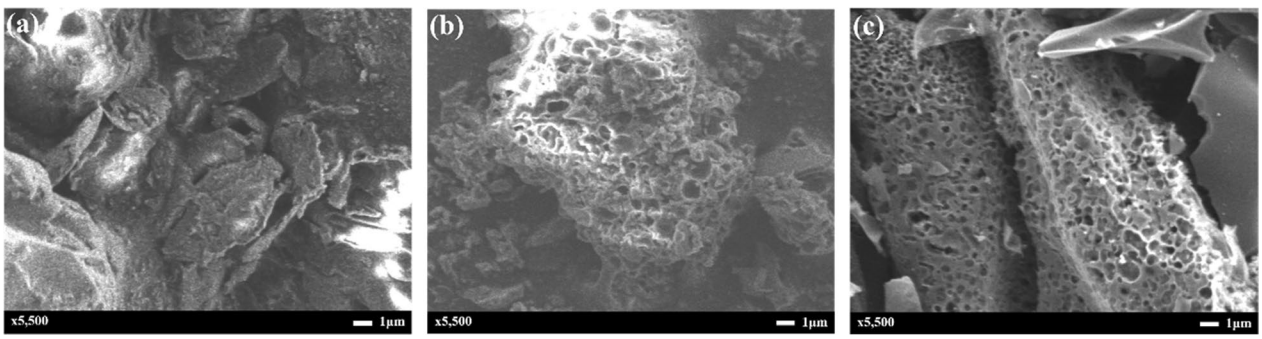

Fig. 8 SEM images of solid residues (magnification = 5500). **a** WS **b** C200/60 **c** C200/60-AC

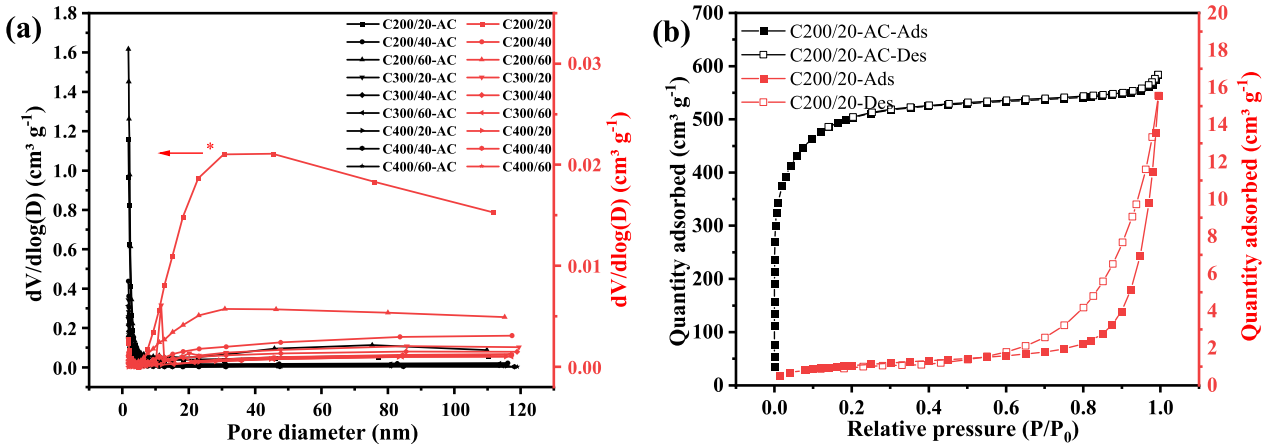

*Pore size from mesoporous to microporous

Fig. 9 **a** Pore size distribution of char and activated carbon **b** N_2 adsorption and desorption isotherms of C200/20 and C200/20-AC

Overall, the benefits of the SC-CO_2 pretreatment process were demonstrated.

From the pore size distribution of SC-CO_2 pretreated char and AC (Fig. 9a), it can be seen that the pores of the char after pretreatment at lower temperatures (200 °C and partially 300 °C) were relatively more developed and more mesoporous structures with pore sizes in the range of 10–100 nm, possessing a small number of microporous structures with pore sizes smaller than 2 nm. The char at higher temperatures had lower peaks, and undeveloped pore structures but uniform pore size distribution with a distribution of micropores and mesopores. The AC obtained after KOH activation displayed very developed pores, especially the two samples with the highest specific surface area, C200/20 and C200/60, with peaks of 1.6 and 1.2 $cm^3\ g^{-1}$, respectively. And the pore sizes of the AC were mainly concentrated in micropores with pore sizes less than 2 nm. From the distribution of 2–5 nm pore sizes in Additional file 1: Fig. S2, the microporous and mesoporous structures of ACs were very well developed and concentrated in the microporous structure, while the micropores and mesopores of the chars were very weak or even absent. The N_2 adsorption and desorption isotherms of C200/20 and C200/20-AC are shown in Fig. 9b (other samples in Additional file 1: Fig. S3). The adsorption–desorption curve of the char C200/20 conformed to a Type III isotherm, indicating a non-porous or macroporous solid material. The curve lacked an inflection point, suggesting the absence of identifiable monolayer formation. The interaction between the adsorbent material and the adsorbate gas was relatively weak, with adsorbate molecules congregating around the most attractive sites on the surface. The sample exhibited limited adsorption capacity at the saturation pressure point ($P/P_0 = 1$). The adsorption–desorption curve of the AC sample C200/20-AC exhibited a typical Type I isotherm, characteristic of adsorption curves for microporous materials. At very low P/P_0 values, there was a sharp increase in adsorption, primarily due to the enhanced interaction between the adsorbent and adsorbate within the narrow micropores, leading to the filling of these micropores at extremely low relative pressures. The subsequent curve was horizontal or nearly horizontal, with adsorption approaching a limiting value, typical of Langmuir isotherms. The saturation of adsorption was due to the constraints imposed by the volume of micropores into which the adsorbed gas can enter, but not due to the internal surface area. When the saturation pressure was reached ($P/P_0 > 0.99$), adsorbate condensation might occur, leading to an upward turn in the curve. And it was obvious that the adsorption capacity of AC was much higher than char.

3.8 Methylene blue adsorption experiments

MB was chosen as the testing index, and adsorption experiments were conducted to assess the adsorption characteristics of the prepared ACs, both under SC-CO_2 atmospheres and N_2 control conditions. The adsorption kinetics of the ACs were calculated and analyzed based on the obtained results. The adsorption curves of AC on MB are shown in Fig. 10a, b. The saturated adsorption of MB dye by AC adsorbent materials decreased with increasing pretreatment temperature and decreased with increasing pretreatment time at the same pretreatment temperature (except for C300/40-AC and C300/60-AC). Sample C200/20-AC had the highest saturated adsorption of 540.0 mg g^{-1}, while the directly activated WS sample WS-AC had a saturated adsorption of 211.5 mg g^{-1}. The highest saturated adsorption of the N_2 control group over 24 h was found in N200/20-AC,

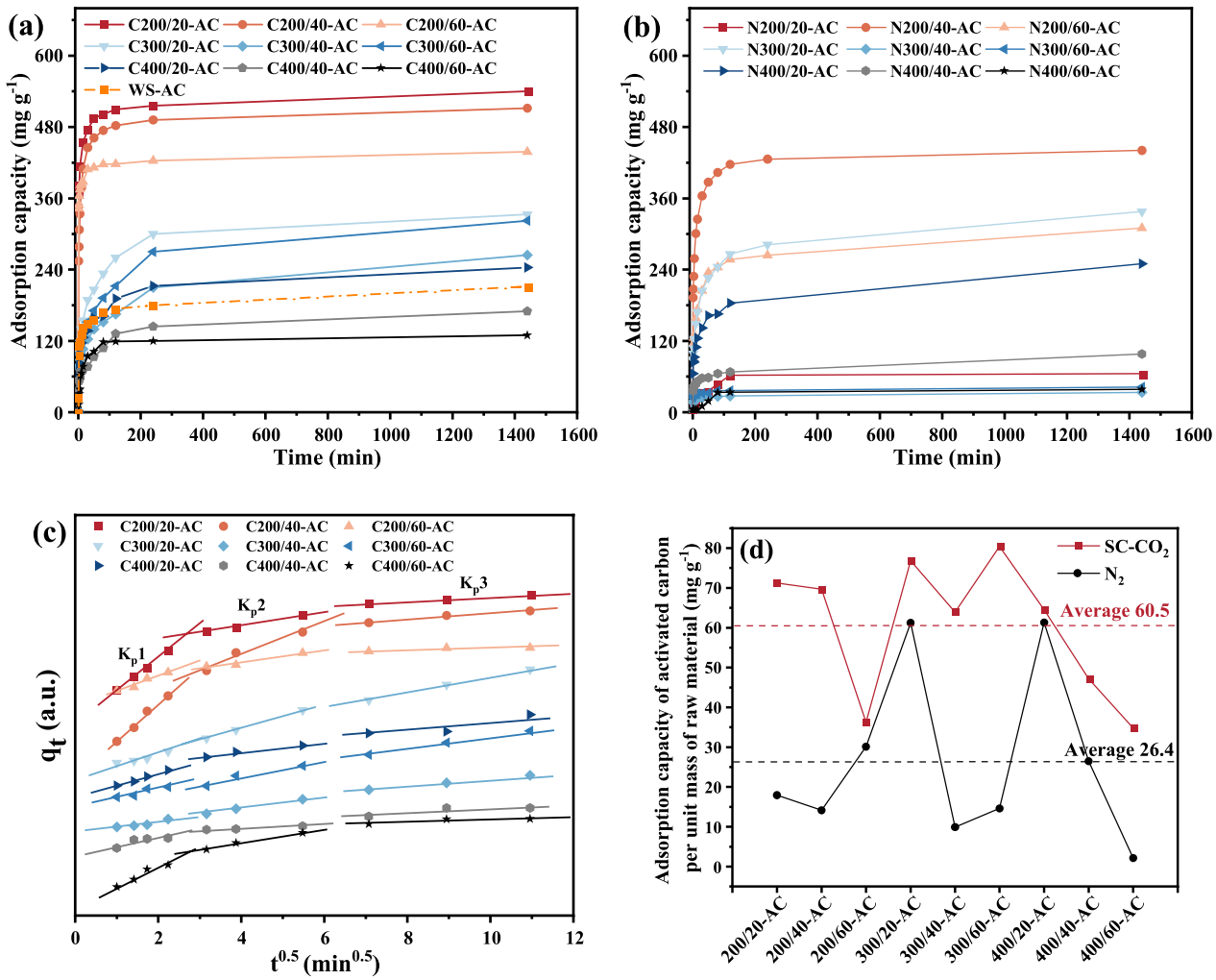

Fig. 10 **a** Adsorption curves for MB of SC-CO_2 pretreated activated carbon and WS-AC **b** Adsorption curves of N_2 pretreated activated carbon **c** Intraparticle diffusion equation for the adsorption of MB by activated carbon **d** Saturated adsorption of MB per unit mass of WS feedstock

which reached 440.7 mg g^{-1}. The adsorption rate of the AC samples prepared by the control group was very slow, for example, N300-AC still did not reach the saturation adsorption amount for 24 h. And the lowest saturated adsorption capacity of AC prepared by SC-CO_2 pretreatment was 129.5 mg g^{-1}, while that of the N_2 control group was only 33.3 mg g^{-1}. So, it is obvious that SC-CO_2 pretreatment had a strong contribution to improve the adsorption performance of AC prepared from biomass. It should be noted that the adsorption performance of AC on MB dye was not necessarily positively correlated with the specific surface area of the sample, because there were also chemical sites on the surface of AC that were active on MB dye, for example, functional groups, such as –OH, –NH, N–O, which could promote the chemical binding of positively charged dye molecules to the surface of AC (Yao et al. 2020), and the high specific surface area and high density microporous structure could improve the mass transfer efficiency. In order to evaluate the performance of AC prepared by SC-CO_2 pretreatment, we searched for studies on other biomass-based AC preparation methods in recent years and listed their preparation methods, specific surface areas, and adsorption capacities of MB in Additional file 1: Table S5. The BET specific surface area of the AC prepared in this work can be seen to possess an advantage compared with other studies. The adsorption effect for MB has an outstanding advantage and it can be concluded that the AC pretreated by SC-CO_2 has a strong performance for wastewater treatment.

The results of the adsorption kinetic analysis (pseudo-first-order equation, pseudo-second-order equation, and intraparticle diffusion equation) of the AC prepared by SC-CO_2 pretreatment followed by KOH activation are presented in Additional file 1: Table S6. The R^2 values of the pseudo-first-order kinetic model were

0.66041- 0.96835, while the R^2 values of the pseudo-second-order kinetic model were 0.99645–0.99997. Therefore, the kinetics of the adsorption of MB by the AC were better represented by the pseudo-second-order model, which indicated that the adsorption of MB by the AC material was chemisorptive. Chemisorption limited the rate of adsorption, where valence forces were created by electron sharing or exchange between the adsorbent and the adsorbate (García et al. 2014). The intra-particle diffusion diagram (Fig. 10c) showed that the adsorption of MB dye on AC basically followed three steps and $K_p1 > K_p2 > K_p3$, indicating a decrease in the rate of molecular diffusion. At first, the MB molecules rapidly occupied the surface of the AC from solution and entered the pores described by K_p2 when the surface adsorption sites were saturated and the rate was further reduced as the adsorption was saturated and the diffusion resistance increased. After the molecules had entered the pores described by K_p3, the diffusion rate was very low and slowly reached saturation (Mohammed et al. 2015).

To investigate the common effects of different treatment processes, considering the yield and adsorption capacity of AC in the two-step method, the saturated adsorption capacity of AC prepared from the unit mass of WS feedstocks for MB was calculated (Fig. 10d). From the results, it could be observed that under any pretreatment conditions, the adsorption capacity of AC prepared from the unit mass of WS in SC-CO_2 atmosphere was higher than that in N_2. Furthermore, due to the influence of the yield, the maximum adsorption capacity of AC prepared from the unit mass of WS appeared at C300/60, reaching 80.4 mg g^{-1}. In summary, using SC-CO_2 pretreatment of biomass for two-step AC preparation offers significant advantages.

4 Conclusion

This study successfully prepared biochar adsorption material with a rich pore structure, high specific surface area, and strong adsorption capacity using a two-step method involving SC-CO_2 pretreatment and KOH activation. Pretreatment with SC-CO_2 under mild conditions resulted in a rough and porous surface structure of the char, which also retained a large number of functional groups providing chemically active sites for the activation step, leading to a more efficient activation and an increase in the total yield. In comparison to the direct activation of WS, the specific surface area increased by 192%, and the total yield increased by 72% under the optimal specific surface area condition. Compared to activated carbon prepared with N_2 pretreatment, the maximum specific surface area increased by 18%, and the maximum adsorption capacity for MB increased by 23%. The optimal pretreatment conditions (at 200 ℃ for 20 min) in this work were mild and energy-efficient. Additionally, the preparation process of samples with the highest specific surface area generated economically valuable organic by-products with high content. The SC-CO_2 pretreatment of biomass has a significant impact on the production of high-specific-surface-area activated carbon, providing a feasible solution for the reuse of WS waste and the treatment of wastewater containing dyes.

Supplementary Information

The online version contains supplementary material available at https://doi.org/10.1007/s42773-024-00302-9.

Additional file 1: Table S1. Elemental analysis of activated carbon. **Table S2.** Summary of FT-IR peaks/band assignment. **Table S3.** Layer diameter and stack height of aromatic lamellae and layer spacing. **Table S4.** Pore characteristics of the samples. **Table S5.** BET surface area and MB adsorption properties of activated carbons prepared by different activation methods. **Table S6.** Adsorption kinetics of MB on activated carbon prepared by SC-CO_2 pretreatment. **Fig. S1.** Gaussian fitting 002 and 100 peaks for C400/60. **Fig. S2.** Pore size distribution from 1.5nm to 5nm of biochars. **Fig. S3.** N_2 adsorption isotherms and pore size distributions of biochars. **a** Absorption and desorption curves of char **b** Absorption and desorption curves of activated carbon.

Acknowledgements
The authors gratefully acknowledge the financial support provided by the National Natural Science Foundation of China (52242609).

Author contributions
ZZ: conceptualization, data curation, investigation, methodology, project administration, supervision, validation, visualization, writing—original draft, writing—review and editing; YL: Methodology, Investigation, Visualization, Formal analysis; WW: Methodology, Investigation, Visualization, Formal analysis; JS: Methodology, Investigation, Visualization, Formal analysis; HJ: Methodology, project administration, supervision, validation, visualization, writing—original draft, writing—review and editing.

Funding
This work is supported by the National Natural Science Foundation of China (52242609).

Data availability
The data that support the findings of this study are available from the corresponding author upon reasonable request.

Declarations

Competing interests
The authors declare that they have no competing interests regarding the publication of this paper.

Author details
[1]State Key Laboratory of Multiphase Flow in Power Engineering, Xi'an Jiaotong University, Xi'an 710049, People's Republic of China.

Received: 26 September 2023 Revised: 30 December 2023 Accepted: 6 January 2024
Published online: 26 January 2024

References

Albarelli JQ, Rabelo RB, Santos DT, Beppu MM, Meireles MAA (2011) Effects of supercritical carbon dioxide on waste banana peels for heavy metal removal. J Supercrit Fluids 58(3):343–351

Badgujar KC, Dange R, Bhanage BM (2021) Recent advances of use of the supercritical carbon dioxide for the biomass pre-treatment and extraction: a mini-review. J Indian Chem Soc 98(1):100018

Balahmar N, Mokaya R (2019) Pre-mixed precursors for modulating the porosity of carbons for enhanced hydrogen storage: towards predicting the activation behaviour of carbonaceous matter. J Mater Chem A 7(29):17466–17479

Butterman HC, Castaldi MJ (2010) Biomass to fuels: impact of reaction medium and heating rate. Environ Eng Sci 27(7):539–555

Egbosiuba TC, Abdulkareem AS, Kovo AS, Afolabi EA, Tijani JO, Auta M, Roos WD (2020) Ultrasonic enhanced adsorption of methylene blue onto the optimized surface area of activated carbon: adsorption isotherm, kinetics and thermodynamics. Chem Eng Res Des 153:315–336

El-Bery HM, Saleh M, El-Gendy RA, Saleh MR, Thabet SM (2022) High adsorption capacity of phenol and methylene blue using activated carbon derived from lignocellulosic agriculture wastes. Sci Rep 12(1):5499

Farrow TS, Sun C, Snape CE (2015) Impact of CO_2 on biomass pyrolysis, nitrogen partitioning, and char combustion in a drop tube furnace. J Anal Appl Pyrol 113:323–331

Gao M, Xu F, Li S, Ji X, Chen S, Zhang D (2010) Effect of SC-CO_2 pretreatment in increasing rice straw biomass conversion. Biosys Eng 106(4):470–475

García ER, Medina RL, Lozano MM, Hernández Pérez I, Valero MJ, Franco AMM (2014) Adsorption of azo-dye orange II from aqueous solutions using a metal-organic framework material: iron-benzenetricarboxylate. Materials 7(12):8037–8057

González-García P (2018) Activated carbon from lignocellulosics precursors: a review of the synthesis methods, characterization techniques and applications. Renew Sustain Energy Rev 82:1393–1414

Hanaoka T, Sakanishi K, Okumura Y (2012) The effect of N_2/CO_2/O_2 content and pressure on characteristics and CO_2 gasification behavior of biomass-derived char. Fuel Process Technol 104:287–294

Jiang J, Yang W, Cheng Y, Liu Z, Zhang Q, Zhao K (2019) Molecular structure characterization of middle-high rank coal via XRD, Raman and FTIR spectroscopy: implications for coalification. Fuel 239:559–572

Jiang F, Cao D, Hu S, Wang Y, Zhang Y, Huang X, Zhao H, Wu C, Li J, Ding Y, Liu K (2022a) High-pressure carbon dioxide-hydrothermal enhance yield and methylene blue adsorption performance of banana pseudo-stem activated carbon. Biores Technol 354:127137

Jiang K, Zhang B, Wang W, Jin H (2022) Effect of the variable physical properties on sub- and supercritical CO_2 flowing over a stationary spherical particle. Phys Fluids 34(10).

Kawamoto H (2017) Lignin pyrolysis reactions. J Wood Sci 63(2):117–132

Keiluweit M, Nico PS, Johnson MG, Kleber M (2010) Dynamic molecular structure of plant biomass-derived black carbon (Biochar). Environ Sci Technol 44(4):1247–1253

Kumar A, Jena HM (2016) Removal of methylene blue and phenol onto prepared activated carbon from Fox nutshell by chemical activation in batch and fixed-bed column. J Clean Prod 137:1246–1259

Liu G, Zhang L (2023) Preparation and process optimization of polyaminated walnut shell adsorbent. Petrochem Technol 52(5):645–651

Liu Q, Wang S, Zheng Y, Luo Z, Cen K (2008) Mechanism study of wood lignin pyrolysis by using TG–FTIR analysis. J Anal Appl Pyrol 82(1):170–177

Liu Z, Zhang F, Liu H, Ba F, Yan S, Hu J (2018) Pyrolysis/gasification of pine sawdust biomass briquettes under carbon dioxide atmosphere: study on carbon dioxide reduction (utilization) and biochar briquettes physicochemical properties. Biores Technol 249:983–991

Mashkoor F, Nasar A (2020) Magsorbents: potential candidates in wastewater treatment technology—a review on the removal of methylene blue dye. J Magn Magn Mater 500:166408

Mohammed N, Grishkewich N, Berry RM, Tam KC (2015) Cellulose nanocrystal–alginate hydrogel beads as novel adsorbents for organic dyes in aqueous solutions. Cellulose 22(6):3725–3738

Naik SN, Goud VV, Rout PK, Dalai AK (2010) Production of first and second generation biofuels: a comprehensive review. Renew Sustain Energy Rev 14(2):578–597

Om Prakash M, Raghavendra G, Panchal M, Ojha S (2020) Thermogravimetric analysis of biochar from Arhar fiber powder prepared at different pyrolysis temperatures, Singapore, Springer Singapore

Pusceddu E, Montanaro A, Fioravanti G, Santilli S, Foscolo P, Criscuoli I, Raschi A, Miglietta F (2017) Comparison between ancient and fresh biochar samples, a study on the recalcitrance of carbonaceous structures during soil incubation. Int J New Technol Res 3:39–46

Rafatullah M, Sulaiman O, Hashim R, Ahmad A (2010) Adsorption of methylene blue on low-cost adsorbents: a review. J Hazard Mater 177(1):70–80

Santoso E, Ediati R, Kusumawati Y, Bahruji H, Sulistiono DO, Prasetyoko D (2020) Review on recent advances of carbon based adsorbent for methylene blue removal from waste water. Mater Today Chem 16:100233

Shafizadeh F (1982) Introduction to pyrolysis of biomass. J Anal Appl Pyrol 3(4):283–305

Shi Q, Wang W, Zhang H, Bai H, Liu K, Zhang J, Li Z, Zhu W (2023) Porous biochar derived from walnut shell as an efficient adsorbent for tetracycline removal. Biores Technol 383:129213

Tan F, Cheng J, Zhang Y, Jiang X, Liu Y (2022) Genomics analysis and degradation characteristics of lignin by Streptomyces thermocarboxydus strain DF3-3. Biotechnol Biofuels Bioprod 15(1):78

Wang C, Zhang S, Wu S, Sun M, Lyu J (2020) Multi-purpose production with valorization of wood vinegar and briquette fuels from wood sawdust by hydrothermal process. Fuel 282:118775

Wang C, Zhang S, Huang S, Cao Z, Xu J, Lyu J (2021) Effect of hydrothermal treatment on biomass structure with evaluation of post-pyrolysis process for wood vinegar preparation. Fuel 305:121513

Wang W, Zhao Q, Lu B, Shi J, Jin H (2024) Pure hydrogen gas production in a coal supercritical water gasification system with CO2 as transporting medium. Appl Therm Eng 237:121529

Xiao K, Liu H, Li Y, Yi L, Zhang X, Hu H, Yao H (2018) Correlations between hydrochar properties and chemical constitution of orange peel waste during hydrothermal carbonization. Biores Technol 265:432–436

Yahya MA, Al-Qodah Z, Ngah CWZ (2015) Agricultural bio-waste materials as potential sustainable precursors used for activated carbon production: a review. Renew Sustain Energy Rev 46:218–235

Yan X, Wang D, Zhang S, Dong X, Yang J, Liu R (2022) Adsorption performance of modified walnut shell adsorbent to Pb^{2+}. J Qingdao Agric Univ (Nat Sci) 39(4):298–303

Yang L, Wang N, Li X (2022) Adsorption of acid fuchsin by walnut shell activate carbon in light and microwave. N Chem Mater 50(11):212–215

Yao X, Ji L, Guo J, Ge S, Lu W, Cai L, Wang Y, Song W, Zhang H (2020) Magnetic activated biochar nanocomposites derived from wakame and its application in methylene blue adsorption. Biores Technol 302:122842

Yi Z, Li C, Li Q, Zhang L, Zhang S, Wang S, Qin L, Hu X (2022) Influence of CO_2 atmosphere on property of biochar from pyrolysis of cellulose. J Environ Chem Eng 10(3):107339

Zhang H, Wu S (2014) Enhanced enzymatic cellulose hydrolysis by subcritical carbon dioxide pretreatment of sugarcane bagasse. Biores Technol 158:161–165

Zhao C, Jiang E, Chen A (2017) Volatile production from pyrolysis of cellulose, hemicellulose and lignin. J Energy Inst 90(6):902–913

Zhou C, Ge Z, Wang Y, Shang F, Guo L (2023) Experimental study on supercritical carbon dioxide gasification of biomass. Carbon Neutral 2(1):2

Zhu S, Bai Y, Luo K, Hao C, Bao W, Li F (2017) Impacts of CO_2 on char structure and the gasification reactivity. J Anal Appl Pyrol 128:13–17